

Sub-millikelvin station at Synergetic Extreme Condition User Facility

Zhi Gang Cheng(程智刚), Jie Fan(樊洁), Xiunian Jing(景秀年), Li Lu(吕力)
Citation: Chin. Phys. B . 2018, 27(7): 070702. **doi:** 10.1088/1674-1056/27/7/070702

Journal homepage: http://cpb.iphy.ac.cn; http://iopscience.iop.org/cpb

What follows is a list of articles you may be interested in

Cryogenic amplifier with low input-referred voltage noise calibrated by shot noise measurement

Wuhao Yang(杨伍昊), Jian Wei(危健)
Chin. Phys. B . 2018, 27(6): 060702. **doi:** 10.1088/1674-1056/27/6/060702

4.3 THz quantum-well photodetectors with high detection sensitivity

Zhenzhen Zhang(张真真), Zhanglong Fu(符张龙), Xuguang Guo(郭旭光), Juncheng Cao(曹俊诚)
Chin. Phys. B . 2018, 27(3): 030701. **doi:** 10.1088/1674-1056/27/3/030701

Crystal structure and thermochemical properties of phase change materials bis(1-octylammonium) tetrachlorochromate

Lu Dong-Fei, Di You-Ying, He Dong-Hua
Chin. Phys. B . 2012, 21(8): 080702. **doi:** 10.1088/1674-1056/21/8/080702

TOPICAL REVIEW — Synergetic Extreme Condition User Facility: Breakthroughs and opportunities for the research of physical science

Sub-millikelvin station at Synergetic Extreme Condition User Facility*

Zhi Gang Cheng(程智刚)[1,†], Jie Fan(樊洁)[1], Xiunian Jing(景秀年)[1], and Li Lu(吕力)[1,2]

[1] *Beijing National Laboratory for Condensed Matter Physics, Institute of Physics, Chinese Academy of Sciences, Beijing* 100190, *China*
[2] *School of Physical Sciences, University of Chinese Academy of Sciences, Beijing* 100190, *China*

(Received 18 February 2018; revised manuscript received 4 May 2018; published online 1 June 2018)

The Institute of Physics, Chinese Academy of Sciences, is in charge of the construction of the Synergetic Extreme Condition User Facility (SECUF) in Huairou, Beijing. The SECUF is a comprehensive facility focused on providing extreme physical conditions for scientific research, including an ultralow temperature, ultrahigh pressure, ultrahigh magnetic field, and ultrafast laser. The ultralow temperature will be realized by the sub-millikelvin (sub-mK) station, whose main component is an adiabatic nuclear demagnetization refrigerator (ANDR). The refrigerator is designed to have a base temperature below 1 mK and a magnetic field up to 16 T for experiments, as well as a characteristic parameter of $B/T \geqslant 10^4$ T/K. In this review, we introduce adiabatic nuclear demagnetization refrigeration, thermometry from 10 mK to sub-mK, the properties and parameters of the ANDR of the SECUF, and related prospective research topics.

Keywords: adiabatic nuclear magnetization, thermometry, superfluid ^{3}He, fractional quantum Hall effects

PACS: 07.20.Mc, 07.20.Dt, 67.30.H–, 73.43.–f **DOI:** 10.1088/1674-1056/27/7/070702

1. Introduction

The liquefication of ^{4}He by Heike Kamerlingh Onnes in 1908 decreased its temperature to the atmospheric boiling point, 4.215 K, and allowed people to study ultralow-temperature physics. From here, people reduced the temperature further using a variety of methods. For example, reducing the vapor pressure of liquid ^{4}He can lower its boiling point to ~ 1 K. Applying the same technique to liquid ^{3}He and a circulating ^{3}He–^{4}He mixture yields base temperatures of ~ 300 mK and ~ 10 mK, respectively. At a lower temperature, more exotic physical phenomena were observed. The first evidence of superconductivity was observed at 4.19 K in mercury by Onnes.[1] Other notable observations include the superfluidity of ^{4}He at 2.17 K,[2] the integer quantum Hall effect (IQHE) at 1.5 K,[3] and the fractional quantum Hall effect (FQHE) at temperatures as low as 0.48 K.[4]

Low-temperature physics is an important branch of condensed-matter research. A fundamental concept in condensed-matter physics is "order", which indicates how matter behaves collectively and coherently. The ideal condition to probe order is the systems set at the ground states. However, this requires $T = 0$ because a finite temperature always introduces thermal excitations and fluctuations that perturbate orders. If the temperature is too high, these perturbations are too strong to preserve the order, effectively submerging or destroying intrinsic properties of the system. As the temperature is reduced, the order starts to emerge, giving rise to exotic quantum phenomena. One can consider the fluctuation of thermal energy $k_B T$ as the resolution for probing the energy structure of a system. A lower T yields better resolution to distinguish fine structures. Take the FQHE for instance: the $\nu = 1/3$ state has a gap up to 10 K, while the gap of the $\nu = 5/2$ state is < 0.6 K.[5–8] The former can be observed at ~ 1 K, whereas the latter is only observed below ~ 0.1 K. New order can start to emerge as the temperature is lowered. For example, liquid ^{4}He remains in the normal phase above 2.17 K; below this temperature, superfluidity occurs. In the superfluid phase, ^{4}He atoms coherently act as a macroscopic quantum system. More interestingly, superfluidity also exists in fermionic liquid ^{3}He via a similar (but not the same) paring mechanism to that of conventional superconductors. The exotic phase exists at far lower temperatures, lower than 2 mK. The aforementioned two phases are the most typical physical systems that require low temperatures to be realized, but low-temperature physics is not limited to these: it includes a broad range of interesting and important topics, such as strongly correlated electron systems, superconductivity, quantum transport in reduced dimensions, quantum phase transitions, and quantum computations. These topics are pivotal not only for understanding fundamental physics but also for developing the

*Project supported by the National Basic Research Program of China (Grant Nos. 2016YFA0300601, 2015CB921402, 2011CB921702, and 2009CB929101), the National Natural Science Foundation of China (Grant Nos. 11527806, 91221203, 11174340, 11174357, and 91421303), and the Strategic Priority Research Program B of the Chinese Academy of Sciences (Grant No. XDB07010100). Z.G.C. acknowledges the support from Hundreds Talent Program, Chinese Academy of Sciences.

†Corresponding author. E-mail: zgcheng@iphy.ac.cn

© 2018 Chinese Physical Society and IOP Publishing Ltd

technology.

Considering its importance for physical science, the implementation of ultralow-temperature facilities is crucial and urgent. Currently, the dilution refrigerator is the most common facility in laboratories for reaching the ultralow-temperature region of < 10 mK. Owing to automatic controlling modules and successful commercialization, the operation of dilution refrigerators has been significantly simplified, with even knowledge of He physics being unnecessary. On the other hand, the skyrocketing price of liquid He urges manufacturers to develop cryogen-free dilution refrigerators, which replace the 1 K pot with a Joule–Thomson chamber or employ a high-pressure technique to condense the ^{3}He/^{4}He mixture. The cryogen-free dilution refrigerator not only has financial advantages but also makes the experiment immune from any unpredicted shortage of liquid He. However, as mentioned previously, some studies require temperatures below the range of dilution refrigerators, such as FQHE states with particular filling factors or superfluid ^{3}He. Adiabatic nuclear demagnetization refrigeration is an effective technique for such low temperatures. Materials with nuclear spins are used to make a two-ensemble system: lattice and nuclear spins. The entropy of the nuclear spins is reduced in advance at the base temperature of a dilution refrigerator, and the entropy of the lattice can be adiabatically transferred into the nuclear ensemble, generating cooling power in the lattice system. Details of the technique are briefly introduced in the next section.

The Synergetic Extreme Condition User Facility (SECUF) is planned as a comprehensive facility project in Huairou, Beijing, that aims to implement an ultralow temperature, ultrahigh pressure, ultrahigh magnetic field, and ultrafast light source for research topics in physical and chemical sciences. The sub-millikelvin (sub-mK) station is an important part of this project. The facility will be the main platform in the SECUF for conducting research on quantum computation and quantum information, including the fabrication, testing, and development of hardware for quantum computation. In addition, the facility can be used for other fundamental research, such as superfluid ^{3}He, quantum spin liquid, and relevant studies requiring sub-mK conditions.

2. Adiabatic nuclear demagnetization refrigerator

In this section, we briefly describe the operation of an adiabatic nuclear demagnetization refrigerator (ANDR) and introduce the one planned for the sub-mK station in the SECUF.

2.1. Demagnetization refrigeration

Consider paramagnetic ions in a solid with a magnetic moment μ. At a sufficiently high temperature where thermal energy $k_{\mathrm{B}}T$ is larger than the interaction energy between moments ε_m, the ions can be viewed as independent and in paramagnetic phase. Their total angular momentum J contributes a magnetic disorder entropy of $S = R \cdot \ln(2J+1)$. Spontaneous magnetic ordering occurs as the temperature is reduced to $k_{\mathrm{B}}T = \varepsilon_m$. The magnetic moments are oriented in a preferred direction, reducing the magnetic disorder entropy. This can also occur at high temperatures under a magnetic field.

Thus, the refrigeration method exploits the magnetic disorder entropy. Figure 1 shows the process of adiabatic demagnetization refrigeration: the magnetic field is increased from 0 to B_{i} at the initial temperature T_{i} to drive the magnetic moments into an ordered state (from A to B). The magnetic disorder entropy S is reduced during this process, and the generated heat is drained to a thermal bath. Then, the demagnetization stage is thermally isolated from the thermal bath, and the magnetic field is ramped down to B_{f}. By making this process adiabatic, the entropy of the system remains constant, but the entropy of the lattice is transferred to the nuclear spin system, effectively reducing the lattice temperature. Considering an ensemble of N_0 magnetic moments within a magnetic field $\boldsymbol{B}$, the Zeeman energy of one moment is given by $\varepsilon_m = g\mu_\alpha mB$, where the index $\alpha = \mathrm{b}$ for the Bohr magneton of electrons, and $\alpha = \mathrm{n}$ for the magneton of nuclui; m is the angular momentum quantum number for the z-direction; and g is the Lande factor. Because the partition function $Z = \left(\sum_{m=-J}^{+J} \mathrm{e}^{-\frac{\varepsilon_m}{k_{\mathrm{B}}T}}\right)^{N_0}$ for N_0 magnetic moments is a function of B/T, the magnetic disorder entropy $S = R \cdot \frac{\partial(T\ln Z)}{\partial T} = R \cdot \left(\ln Z + \left(\frac{T}{B}\right)\frac{\partial(\ln Z)}{\partial(T/B)}\right)$ is also a function of B/T. Thus, B/T is conserved during the adiabatic process, and the temperature should decrease and settle at $T_{\mathrm{f}} = \frac{B_{\mathrm{f}}}{B_{\mathrm{i}}}T_{\mathrm{i}}$. Once the demagnetization finishes, the stage slowly warms because of the heat leakage into the demagnetization stage (C to A).

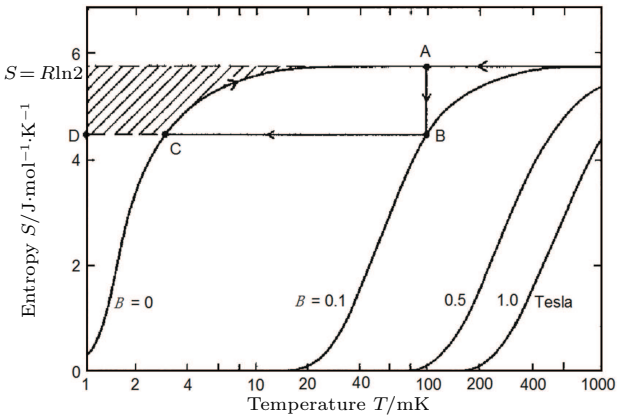


Fig. 1. Temperature dependence of the molar magnetic disorder entropy of a single crystal of CMN under different magnetic fields. Its angular moment is $J = 1/2$, with the entropy $S = R\ln 2$. The entropy decreases at a lower temperature as higher ordering emerges. The ordering appears at a higher temperature with a stronger field. The process A → B → C indicates the process of adiabatic refrigeration. From A to B, the magnetic field is increased at the initial temperature T_{i}. From B to C, the magnetic field is decreased. The temperature decreases to the final temperature T_{f}. From C to A, the temperature is increased gradually owing to the heat leakage into the demagnetization stage. (Regenerated from Ref. [58].)

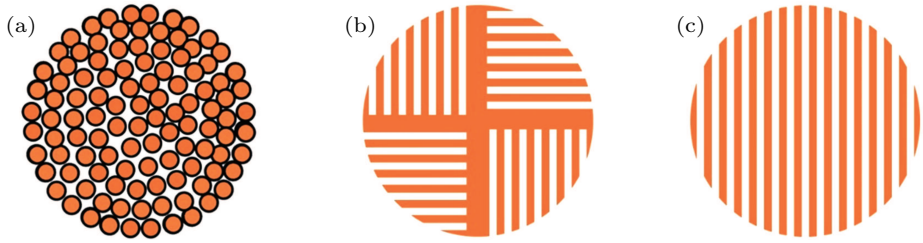


Fig. 2. (color online) Various designs of the copper demagnetization stage.

The aforementioned relationship $B_i/T_i = B_f/T_f$ is invalid in the limit of $B_f \to 0$ because it neglects the interactions between the magnetic moments, which should give a remnant internal field $\boldsymbol{b} = \frac{\mu_0}{4\pi}\sum_i(\frac{\boldsymbol{\mu}_i}{r_i^3} - 3\boldsymbol{r}_i\frac{\boldsymbol{\mu}_i\cdot\boldsymbol{r}_i}{r_i^5})$, where $\boldsymbol{\mu}_i$ and $\boldsymbol{r}_i$ are the magnetic moment and the distance of other moments, respectively. In this limit, the magnetic field that one moment feels is $B_{\text{eff}} = \sqrt{b^2 + B_f^2}$, and the final temperature is $T_f = \frac{\sqrt{b^2+B_f^2}}{B_i}T_i$, yielding a minimum final temperature of $T_{f,\min} = \frac{b}{B_i}T_i$.

Demagnetization refrigeration can be realized with different cooling agents. The interaction energy between moments is given by $\varepsilon_d = \boldsymbol{\mu}\cdot\boldsymbol{b} = \frac{\mu_0\mu}{4\pi}\cdot\sum_i(\frac{\boldsymbol{\mu}_i}{r_i^3} - 3\boldsymbol{r}_i\frac{\boldsymbol{\mu}_i\cdot\boldsymbol{r}_i}{r_i^5})$, so that the onset temperature of the spontaneous magnetic ordering is $T_c \propto \mu^2/r^3$. Paramagnetic salt can be used to reduce the temperature from the kelvin range to the millikelvin range by exploiting the magnetic moment of electrons. Because the nuclear magnetic moment is on the order of 10^{-27} J/T, which is 34 orders of magnitude lower than that of electrons, the T_c for the nuclear moment is far lower, on the order of 0.1 μ K. Therefore, the ANDR operates at a far lower temperature than paramagnetic salt. It usually starts at $T_i \approx 10$ mK and reaches < 1 mK. Because the ANDR requires a low starting temperature, the dilution refrigerator is an ideal facility to precool it. A typical starting field is $B_i = 9$ T, demagnetized to an effective field b of a few millitesla. A superconducting heat switch connects the mixing chamber and the demagnetization stage (see Fig. 3). The switch is turned on during magnetization to serve as a strong thermal link for dumping heat from the cooling agent into the mixing chamber and turned off during demagnetization to isolate the cooling agent.

Several criteria should be considered for the choice of a proper cooling agent, as follows. (i) It should be a good conductor, so that free electrons can facilitate thermal equilibrium between the nuclear system and the lattice. (ii) It must have a relatively large nuclear magnetic moment and thus a large magnetic disorder entropy in the paramagnetic phase. (iii) It should not have a strong internal field b at low temperatures. (iv) It should have large mechanical strength and machinability. Considering these criteria with some compromise, copper and $PrNi_5$ are the most widely used cooling agents for the ANDR.

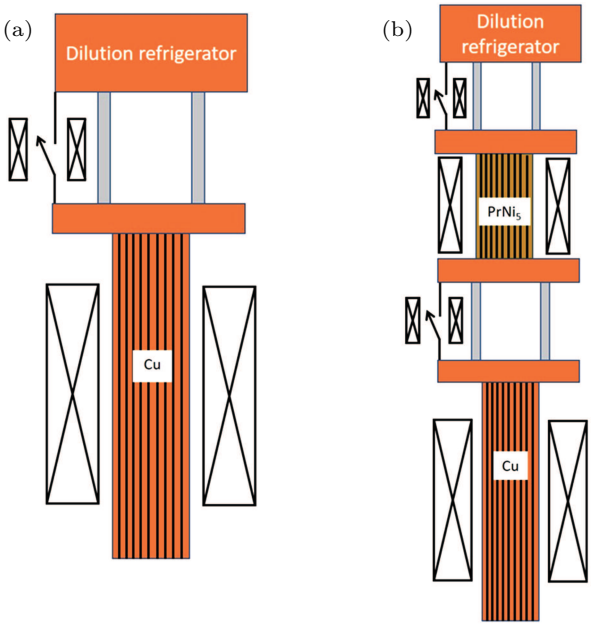


Fig. 3. (color online) Schematics of the demagnetization stage attached to the dilution refrigerator: (a) single Cu stage, (b) hybrid double stage with $PrNi_5$ and Cu.

Because of its good machinability, electrical and thermal conductivities, affordable price, and commercial availability, copper is widely used for demagnetization refrigeration. It has a nuclear magnetic moment of $I = 3/2$. Given its superior conductivity, a large bulk amount of copper should be avoided to prevent eddy currents and heating during demagnetization. One way to do this is by using a bundle of fine copper rods with insulation. However, the defect density is usually high in thin rods, which limits their thermal conductivity. Moreover, the connections to flanges at both ends are difficult to make owing to thermal boundary resistance. Another effective method is to cut slits in a large copper rod and keep the entire stage as one piece (see Fig. 2). This method has the advantages of maintaining the superior mechanical properties and avoiding the trouble of making proper soldering connections. Defects and impurities affect the thermal conductivity of copper (as well as the electrical conductivity, according to the Wiedemann–Franz law). To improve its thermal conductivity, copper should be carefully annealed before installation. With proper annealing, the residual resistivity ratio can be as high as 1000. Additionally, H_2 has been found in copper, and its ortho–para conversion is a significant source of heat leak-

age at ultralow temperatures even when its concentration is low. Even one week after the initial cool down, 1 ppm of H_2 in 1 kg of copper can give rise to 5 nW of heat leakage.[9] Annealing is also effective for decreasing the H_2 concentration. The annealing should be conducted in vacuum. It is advisable to introduce the proper amount of O impurities to seize magnetic impurities, weakening the internal field b. The amount of O should be fine-tuned to prevent extensive oxidation.

The main reduction of the magnetic disorder entropy of copper occurs below 10 mK, requiring an initial temperature of $T_i < 10$ mK. On the other hand, $PrNi_5$, with a nuclear magnetic moment of $I = 5/2$ and thus a larger entropy reduction, undergoes its main entropy reduction between 100 mK and 10 mK, as shown in Fig. 4. Thus, $PrNi_5$ is usually used as an intermediate stage between the mixing chamber and the copper stage in two-stage ANDRs (as shown in Fig. 3(b)) if the base temperature of the dilution fridge is not sufficiently low. In addition to its large magnetic moment, it has a high specific heat, yielding a long holding time at low temperatures. However, it has poor machinability and thermal conductivity. To resolve these disadvantages, $PrNi_5$ is usually used as a bundle of thin rods, and high-purity copper wires should be soldered along the entire length to improve the thermal conductance.

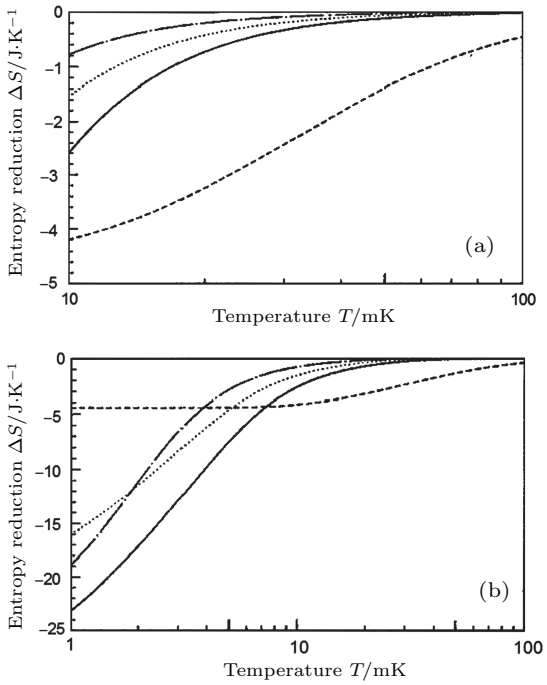


Fig. 4. Nuclear spin entropy reduction of 1.4 mol of Nb (solid line), 1.0 mol of In (dotted line), 2.0 mol of Cu (dotted-dashed line), and 0.3 mol of $PrNi_5$ (dashed line). Panels (a) and (b) plot the same set of data within a different temperature range. The aforementioned amount of each material yields the same volume of refrigerant. (Regenerated from Ref. [9].)

2.2. Thermometry in millikelvin and sub-mK temperature ranges

The ANDR operates in the temperature range of 10 mK to sub-mK. An appropriate thermometry within this range should have not only sufficient sensitivity but also superior thermal contact to the experimental stage. Common types of thermometry include ^{3}He melting curve thermometry (^{3}He-MCT), cerium magnesium nitrate thermometry (CMN), and Pt nuclear magnetic resonance (Pt-NMR) thermometry. ^{3}He-MCT and Pt-NMR thermometry, which are briefly reviewed in this section, will be performed on the sub-mK station at the SECUF.

^{3}He-MCT Both ^{4}He and ^{3}He remain liquid till absolute zero unless pressurized into a solid phase. The extensive liquid phase down to absolute zero makes both isotopes ideal refrigerants. Their melting curves, which also extend to absolute zero, can be used for proper thermometry. For ^{4}He, the melting curve flattens out below ~ 1 K (with a very shallow minimum around 0.7 K), limiting its use in thermometry to higher temperatures. In contrast, the melting curve of ^{3}He does not have a flat region (see Fig. 5); it decreases with decreasing temperature, reaches a minimum of $P_{\min} = 2.93113$ MPa at $T_{\min} = 315.24$ mK, and then starts to increase again. In addition, liquid ^{3}He transitions from a normal liquid to the superfluid A-phase ($P_A = 3.43407$ MPa, $T_A = 2.444$ mK) and then to the superfluid B-phase ($P_{AB} = 3.43609$ MPa, $T_{AB} = 1.896$ mK). Furthermore, solid ^{3}He experiences a Néel transition ($P_N = 3.43934$ MPa, $T_N = 0.902$ K). These fixed points can be used as reference for thermometry calibration. The complete melting curve of ^{3}He is given by the new provisional low-temperature scale (PLTS-2000) down to 0.9 mK.[10]

^{3}He-MCT works when a solid–liquid coexisting state of ^{3}He is present. The density of the coexisting sample should be chosen appropriately to maximize its working range. To prepare a coexisting sample, liquid ^{3}He is pressurized to a relatively high pressure at a high temperature. The temperature is then decreased and hits the melting curve when a solid starts to form. Freezing usually occurs within the capillary, stopping liquid ^{3}He from entering the cell; thus, the density within the cell is kept constant. The solid fraction increases as the temperature cools towards $T_{\min}$. Below $T_{\min}$, the solid starts to melt owing to the negative slope of the melting curve (thus negative latent heat). Complete freezing before reaching $T_{\min}$ and complete melting before reaching the lowest temperature should be avoided to keep the sample on the melting curve. Hence, the density should fall into a proper range: it should be between that of liquid at the lowest temperature (molar volume $V_m = 254$ cm^3/mol) and that of solid at the melting-curve minimum ($V_m = 2495$ cm^3/mol). As shown in Fig. 5, this restriction is translated into a starting zone where liquid can hit the melting curve, i.e., between (765 mK, 3.436 MPa) and (915 mK, 3.781 MPa). The practical upper end should be lower because a large solid fraction, although not 100%, might completely cover the pressure gauge and apply anisotropic stress on it, preventing it from measuring the real hydrostatic

pressure.

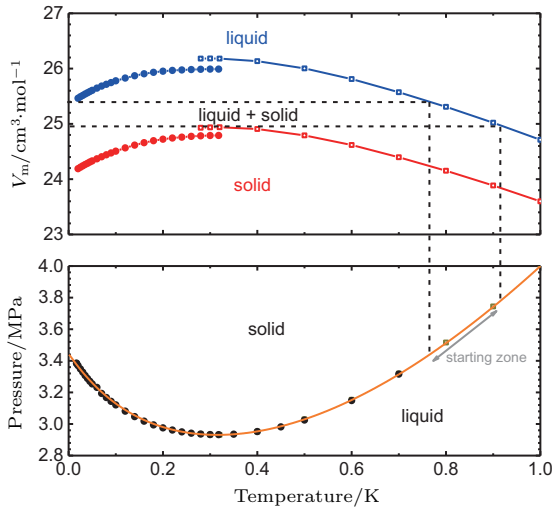


Fig. 5. (color online) Molar volume (top) and melting curve (bottom) of liquid and solid ^{3}He. The solid circles represent data from Ref. [59], and the empty squares represent data from Ref. [60] . The orange curve is generated according to PLTS-2000.[10] The area between the two horizontal dashed lines indicates the density range for MCT. To make the density fall within this range, the temperature at which the sample hits the melting curve should be between the two temperatures indicated by the vertical dashed lines.

Figure 6 schematically shows a device for ^{3}He-MCT. ^{3}He is injected into the MCT cell through a thin capillary, and a Straty–Adams capacitive pressure gauge[11] is used to detect the pressure of the coexisting sample. Here, we wish to emphasize several points. First, coaxial cables must be used for the pressure gauge to avoid extra capacitance between leads. The two bare wires next to the plates should be shielded from each other. Second, because of the notoriously large specific heat of liquid/solid ^{3}He and the significantly large Kapitza resistance at low temperatures, Ag sinters must be installed within the cell to improve the thermal links between the ^{3}He and the MCT cell. Ag particles with average diameter of 70 nm should be packed on the opposite side of the pressure gauge to guarantee proper pressure measurement. Fine copper gauze could be buried into the particles before packing to prevent the sinter from cracking after multiple thermal cycles. Third, the mounting base should be made of copper with gold coating in order to minimize the thermal boundary resistance between the MCT cell and the experimental stage. Fourth, the capillaries to the MCT cell should be carefully heat-sunk at every stage, and their inner diameter should be minimized to reduce the thermal leakage along the liquid He in the capillary. Lastly, the Straty–Adams pressure gauge should be calibrated using a pressure gauge at room temperature by pressurizing the MCT cell with liquid ^{3}He at a relatively high temperature. However, there should be a pressure gradient along the thin capillary, which is presumably constant. A correction should be made to shift the measured melting curve according to its fixed minimum point.

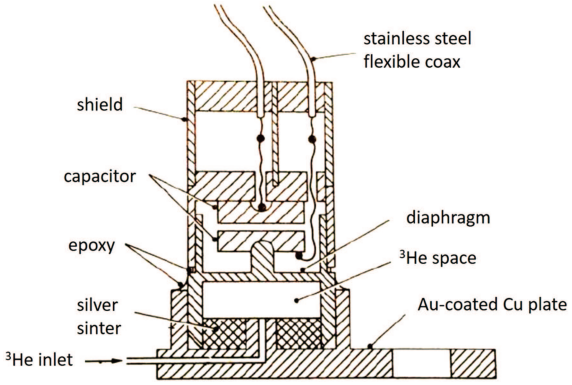


Fig. 6. Design of a cell for ^{3}He-MCT.

Pt-NMR thermometry The ^{3}He MCT temperature range extends to the Néel temperature of solid ^{3}He: T_N = 0904 mK. This barely covers the sub-mK range in which the ANDR mainly operates. To date, the only type of thermometry that covers the sub-mK temperature range is NMR thermometry.[12] Pt, which obeys Curie's law down to this range with a large spin–lattice interaction time constant (τ_1) and a small spin–spin interaction time constant (τ_2), is an ideal material for NMR thermometry.

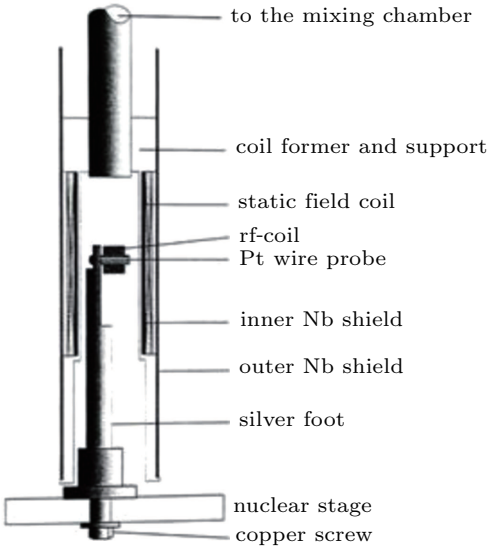


Fig. 7. Design of the pulsed Pt-NMR thermometer.

When a static magnetic field is applied along the z-axis $\boldsymbol{B}_z = B_z\hat{\boldsymbol{z}}$, the nuclear magnetization of Pt is aligned along the field $\boldsymbol{M}_n = M_n\hat{\boldsymbol{z}}$, where $M_n = \chi_n H_z = B_z\lambda_n/\mu_0 T$, and λ_n is the Curie constant. As a short pulse of sinusoidal field is applied in the xy-plane, for instance, $\boldsymbol{B}_y = B_1\sin(\omega t)\hat{\boldsymbol{y}}$ with ω matching the Zeeman splitting ($\hbar\omega = \mu\mu_0 B_z/I$, where μ and I are the relative permeability and the nuclear magnetic moment of Pt, respectively, and μ_0 is the permeability of free space), $\boldsymbol{M}_n$ is tipped from $\hat{\boldsymbol{z}}$ by an azimuthal angle of $\theta = \pi B_1/B_z$ and precesses around $\hat{\boldsymbol{z}}$ at the resonance frequency ω. The precession of the in-plane component causes a potential difference in a pick-up coil $U(t) = \alpha\omega M_n \sin\theta \sin(\omega t)\, \mathrm{e}^{-t/\tau_2}$, where α

is a coil-related constant, and $M_n \propto 1/T$. After being amplified and integrated over the decay time, $U(t)$ is transformed into a signal $S \propto 1/T$, making it a proper candidate for thermometry. To determine the other parameters, one should calibrate the thermometry at a higher known temperature with the assumption that the spin–spin interaction time constant τ_2 is temperature-independent. A block diagram of Pt-NMR thermometry is shown in Fig. 8, and additional details regarding a typical pulsed NMR measurement are presented in Ref. [13]. The same coil can be used for tipping and pick-up, as the tipping and measurement are not simultaneous.

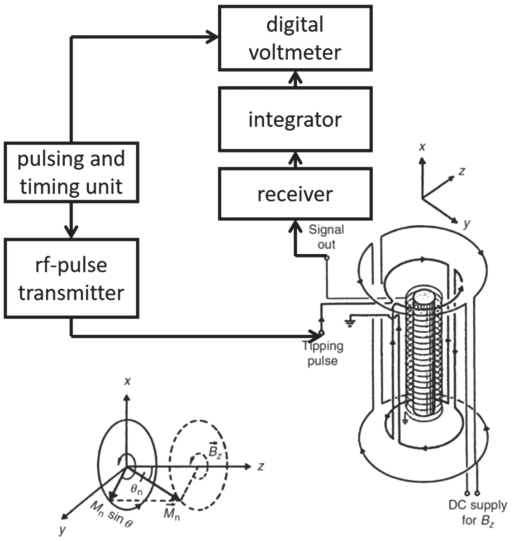


Fig. 8. (a) Schematic of pulsed Pt-NMR thermometry. (b) Block diagram of Pt-NMR thermometry and a drawing of the coil assembly. The tipping and pick-up coils are separate in the drawing but can be realized with one coil in principle. The figure is adapted from Ref. [9].

To conduct pulsed Pt-NMR thermometry in the sub-mK range and achieve reliable results, several requirements must be satisfied. The NMR signal scales with $\sin\theta$, i.e., the tipping angle of the nuclear magnetization away from the z-direction. A larger tipping angle should yield better resolution. However, the tipping field induces an eddy current within Pt, potentially introducing self-heating. Additionally, the tipping M_n effectively increases the temperature of the nuclear system from T_n to $T_n \cos^{-1}\theta$, with an increment of $\Delta T = T_n\left(\cos^{-1}\theta - 1\right) \approx T_n\theta^2/2$ for small θ. Therefore, a tradeoff between the signal amplitude and the heating effect should be achieved. The radio-frequency field of the tipping pulse also introduces eddy-current heating and increases the electron temperature,[14,15] which should be carefully considered and minimized. Moreover, small samples should always be used, not only to keep the eddy-current heating small but also to make the electromagnetic field fully penetrate the sample. The penetration depth is given by $\delta = \left(\frac{2\rho}{\mu_0\omega}\right)^{1/2}$, where ρ is the resistivity of Pt. The typical size of Pt is on the order of 10 μm; thus, bundles of thin wires or powders are often used. On the other hand, the thermal link between the Pt sample and the experimental stage should be strong, and a highly pure Ag post is often used (see Fig. 7). Additionally, proper magnetic shielding is crucial for the thermometry. A double-layer Nb shield is used for the Pt-NMR thermometer of the ANDR at the SECUF.

3. Prospective research on ANDR

The unique sub-mK temperature realized by the ANDR makes it a special tool for a broad range of research. Exotic quantum phenomena, many of which can only be observed at an ultralow temperature, are the main projects to be conducted using the ANDR at the SECUF. In this section, we review two typical research topics that are closely related to or only emergent in the sub-mK temperature range: superfluid ^{3}He and specific states of the FQHE. We apologize for our limited knowledge if any related research field is missed. We cannot review all studies conducted at ultralow temperatures owing to the length limit of this article. However, all research projects for which a sub-mK temperature is an essential experimental condition are welcomed on the ANDR at the SECUF.

3.1. Superfluid ^{3}He

^{3}He shares some features with its isotope ^{4}He, for example, large zero-point motion, remaining in the liquid state down to absolute zero, and superfluidity at low temperatures. However, being a fermion with a nuclear spin of 1/2, it features significant uniqueness: it obeys Fermi liquid theory in its normal liquid phase, and its bulk superfluid phase is divided into two phases: 1) an A-phase at the high-temperature and high-pressure corner and 2) a B-phase at a low pressure or temperature. A phase diagram of the superfluid ^{3}He is shown in Fig. 9. With zero magnetic field, liquid ^{3}He enters the A-phase first at T_c for pressures higher than 2.15 MPa. T_c increases with the pressure until it terminates at the melting curve at ($T = 2.79$ mK, $P = 3.44$ MPa). With further cooling, it enters into the B-phase at T_{AB}. For a pressure lower than 2.15 MPa, it directly enters the B-phase, at which T_c extends to 1.04 mK under zero pressure. The P–T_c curve is smooth at the polycritical point (PCP: $T = 2.56$ mK, $P = 2.15$ MPa), where normal liquid, A-phase, and B-phase coexist. The phase diagram is very sensitive to the magnetic field. Once a small field is applied, the PCP disappears, and the A-phase extends to zero pressure through a narrow stripe, meaning that normal liquid ^{3}He has to enter the A-phase before reaching the B-phase for all pressures. Meanwhile, the A-phase splits into the A_1-phase and A_2-phase. The A_1-phase is sandwiched between the normal phase and the A_2-phase, stemming from the melting pressure at $B = 0$, and its width increases with the magnetic field. The A_2-phase is the same as the A-phase at zero field while A_1-phase is half of it, as discussed below.

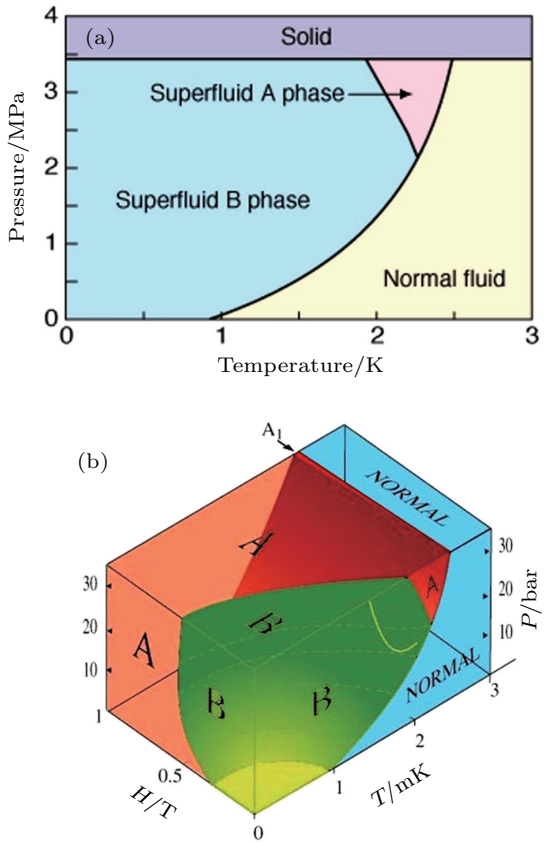


Fig. 9. (color online) (a) Phase diagram of ^{3}He under zero magnetic field. (b) Phase diagram of liquid ^{3}He with variable temperature and magnetic field (figure credit: http://ltl.tkk.fi/images/archive/ab.jpg).

The superfluidity of ^{3}He was accidentally observed by Osheroff, Richardson, and Lee during the study of the magnetic ordering in solid ^{3}He along the melting curve in a Pomeranchuk cell.[16] Making use of the inverted entropy difference between liquid and solid ^{3}He, a solid–liquid coexisting sample was cooled to 1 mK via mechanical compression. Figure 10 shows a compression–release cycle. The temperature was reduced to its minimum (point C) during the compression and increased during the release. There was a kink at point A ($P = 339053$ MPa) during the cooling and another kink at A$'$ during the warming at the same pressure/temperature. Similarly, two jumps occurred at points B and B$'$ ($P = 339279$ MPa). These kinks were first interpreted as the entrance of the solid into a new magnetic-ordering state. However, the following NMR experiment unambiguously proved that it was the liquid, rather than the solid, that transitioned to new phases.[17] The continuity at A and the abrupt jump at B suggest the nature of the second-order transition from the normal phase to the A-phase and the first-order transition from the A-phase to the B-phase. It was confirmed by a specific-heat experiment[18] that there exists a jump in the specific heat at T_c and a mild kink at T_{AB} (see Fig. 11). With a magnetic field, the specific heat exhibits two jumps near T_c, signifying transitions into the A_1 and A_2 phases, respectively, both being second-order transitions. Although superfluid ^{3}He was first observed in a dilution fridge under Pomeranchuk cooling, the ANDR is a far more reliable and convenient cooling method for studies in this field. The ANDR at the SECUF, extending below 1 mK, could be an ideal platform for studies on superfluid ^{3}He.

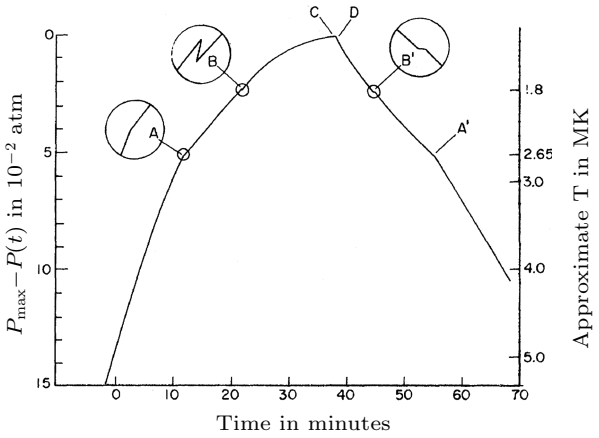


Fig. 10. Pressure and temperature variations during the compression–release cycle within the Pomeranchuk cell containing liquid–solid coexisting ^{3}He. (Regenerated from Ref. [16].)

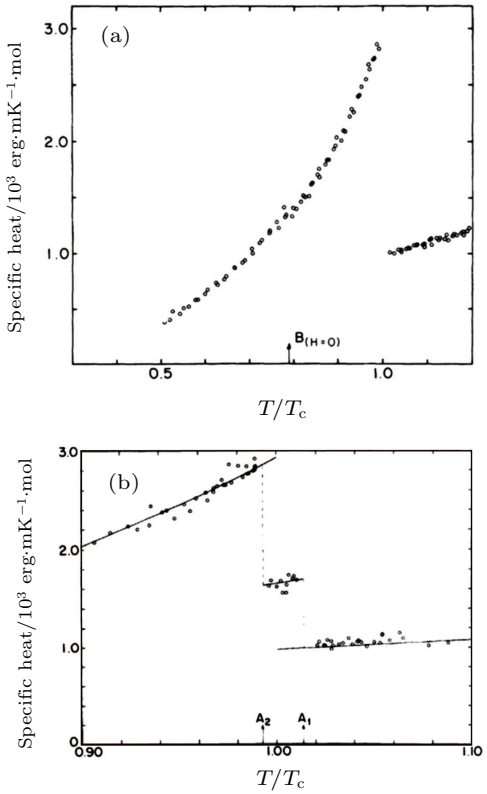


Fig. 11. Specific heat of liquid ^{3}He under (a) zero magnetic field and (b) a field of 8.8 kOe. The arrow in (a) indicates the transition to the B-phase. The arrows in (b) indicate the transition from the normal phase to the A_1 phase and from the A_1 phase to the A_2 phase. (Regenerated from Ref. [18].)

The theory of superfluid ^{3}He was first developed by Leggett,[19] arguing that it is realized by pairing two ^{3}He

atoms into a Cooper pair. However, in contrast to electron pairing in Bardeen–Cooper–Schrieffer (BCS) theory, ^{3}He atoms are regarded as rigid spheres and thus cannot occupy the same position as the s-wave bound state. Instead, they may form bound states with higher angular momentum, starting from p-wave with angular momentum $l=1$ and $l_z=0,\pm1$. Being fermions, spins must form a triplet instead of a singlet to preserve antisymmetry, giving $s=1$, $s_z=0,\pm1$. The order parameter is then represented by a complex 3×3 tensor $A_{\mu i}$ with the index μ in the spin space and i in the orbital space. $A_{\mu i}$ is composed of three parts: the superfluid gap with a phase according to U(1) symmetry $\Delta\,\mathrm{e}^{\mathrm{i}\Phi}$, as in the s-wave superfluid state in ^{4}He; the anisotropy in the orbital space described by $\hat{\boldsymbol{l}}=\hat{\boldsymbol{e}}_1\times\hat{\boldsymbol{e}}_2$, where $\hat{\boldsymbol{e}}_1$ and $\hat{\boldsymbol{e}}_2$ are mutually orthogonal unit vectors, and $\hat{\boldsymbol{l}}$ represents the direction of the orbital angular momentum; and the anisotropy in the spin space, which is described by the vector $\boldsymbol{d}$ as

$$\begin{aligned}|\,\Phi\rangle &= \frac{1}{\sqrt{2}}\big[(d_x-\mathrm{i}d_y)\,|\uparrow\uparrow\rangle \\ &\quad +(d_x+\mathrm{i}d_y)\,|\downarrow\downarrow\rangle+d_z\,(|\uparrow\downarrow\rangle+|\downarrow\uparrow\rangle)\big] \\ &= \frac{1}{\sqrt{2}}\big[d_x\,(|\uparrow\uparrow\rangle+|\downarrow\downarrow\rangle) \\ &\quad +\mathrm{i}d_y\,(|\downarrow\downarrow\rangle-|\uparrow\uparrow\rangle)+d_z\,(|\uparrow\downarrow\rangle+|\downarrow\uparrow\rangle)\big].\end{aligned}$$

The second equation makes it obvious that $\boldsymbol{d}\cdot\boldsymbol{s}=0$, i.e., $\boldsymbol{d}$ lies in the plane perpendicular to the spin orientation.

Different superfluid phases have different forms of order parameters. The A-phase consists of only $|\uparrow\uparrow\rangle$ and $|\downarrow\downarrow\rangle$. Its order parameter is given as[20]

$$A_{\mu i}=\Delta_{\mathrm{A}}\,\mathrm{e}^{\mathrm{i}\Phi}\hat{d}_\mu\left(\hat{e}_1^i+\mathrm{i}\hat{e}_2^i\right),$$

which conserves spin-rotation symmetry $\mathrm{U}(1)_S$ and a reduced orbital-rotation symmetry $\mathrm{U}(1)_{L-N/2}$ as the rotation of $(\hat{e}_1^i+\mathrm{i}\hat{e}_2^i)$ can be compensated by gauge transformation $\Phi\to\Phi+\delta\Phi$. Its Hamiltonian is given by

$$\mathcal{H}_{\mathrm{A}}=M\,(\boldsymbol{p})\,\tau^3+c_\perp\,(\boldsymbol{\sigma}\cdot\boldsymbol{d})\left(\tau^1\hat{\boldsymbol{e}}_1\cdot\boldsymbol{p}-\tau^2\hat{\boldsymbol{e}}_2\cdot\boldsymbol{p}\right),$$

with the quasiparticle spectrum

$$E_{\mathrm{A}}^2\,(\boldsymbol{p})=M^2\,(\boldsymbol{p})+{c_\perp}^2\left(\boldsymbol{p}\times\hat{\boldsymbol{l}}\right)^2,$$

where τ and σ are the Pauli matrices in the particle–hole space and spin space, respectively; $M\,(\boldsymbol{p})=\frac{p^2}{2m}-\mu$; m is the mass of a ^{3}He atom; μ is the chemical potential; $c_\perp=\Delta_{\mathrm{A}}/p_{\mathrm{F}}$; and p_{F} is the Fermi momentum. The energy diagram for the A-phase is shown in Fig. 12(a). There are two nodes where the energy gap closes on the Fermi surface: $\boldsymbol{p}_\pm=\pm p_{\mathrm{F}}\hat{\boldsymbol{l}}$. The A-phase fits the state proposed by Anderson, Brinkman, and Morel, which was later called the ABM state.[21,22] The A_1-phase exists when a magnetic field is applied. It is spin-polarized, composed of only $|\uparrow\uparrow\rangle$ or $|\downarrow\downarrow\rangle$; thus, it can be viewed as half of the A-phase.

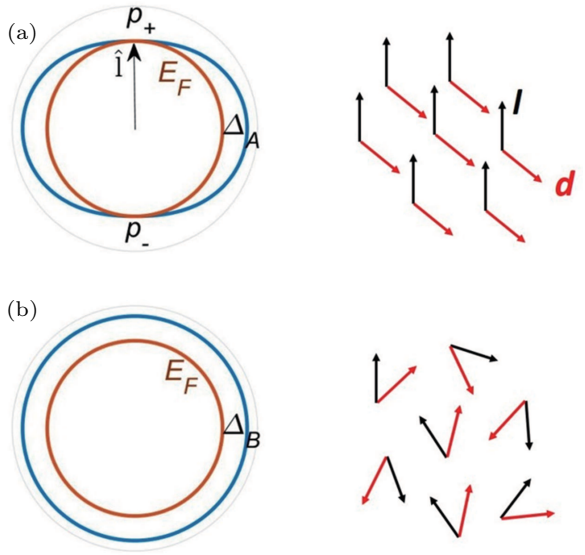


Fig. 12. (color online) (a) Spectrum of A-phase of superfluid ^{3}He with the energy gap closed at two nodes $p_\pm$ and maximized at the equator. There are preferential orientations for the spontaneous orbital angular momentum $\boldsymbol{l}$ and the spin anisotropy $\hat{\boldsymbol{d}}$. (b) Spectrum of the B-phase with an isotropic energy gap. The spin anisotropy orientation $\hat{\boldsymbol{d}}$ is locked to that of the angular momentum, but there is no preferential orientation for the composite.

The B-phase is composed of all three spin configurations. Its order parameter is given by[20]

$$A_{\mu i}=\Delta_{\mathrm{B}}R_{\mu i}\,\mathrm{e}^{\mathrm{i}\Phi},$$

where Δ_{B} is the energy gap, and $R_{\mu i}$ represents the combined action of the spin and orbital rotation. The spin and orbital momenta are locked in the B-phase. The locking reduces two independence symmetries, $\mathrm{SO}(3)_L$ in the orbital space and $\mathrm{SO}(3)_S$ in the spin space, into a combined symmetry $\mathrm{SO}(3)_{L+S}$. Its Hamiltonian is given by

$$\mathcal{H}_{\mathrm{B}}=M\,(\boldsymbol{p})\,\tau^3+c\,(\boldsymbol{\sigma}\cdot\boldsymbol{p})\,\tau^1,$$

with $c=\Delta_{\mathrm{B}}/p_{\mathrm{F}}$, and its spectrum

$$E_{\mathrm{B}}^2\,(\boldsymbol{p})=M^2\,(\boldsymbol{p})+c^2p^2$$

gives an isotropic energy gap, as shown in Fig. 12(b). The B-phase fits the state proposed by Balian and Werthamer, which is called the BW state.[23]

Searching for non-Abelian anyons is an interesting topic in contemporary condensed-matter research. Such quasiparticles are predicted to exist in topological superconductors, which differ from the trivial s-wave pairing superconductors. Proposals have been made to investigate the 5/2 fractional quantum Hall state[24] and Sr_2RuO_4,[25–27] which are suspected as p-wave (-like) superconductors. However, superfluid ^{3}He, as an unambiguous p-wave pairing superfluid, has been overlooked. B-phase ^{3}He is a superfluid counterpart of the three-dimensional topological insulator.[28] With a fully gapped bulk form and a gapless surface, theoretical

prediction shows that it can host the Majorana state at the surface.[29] The existence of the surface state has been experimentally detected via acousticimpedance[30,31] and specific-heat measurements,[32] and this state is interpreted as an Andreev bound state. Further experiments, such as electron spin relaxation,[29] have been proposed to search for evidence of the Majorana state.

On the other hand, the A-phase is a chiral p_x+ip_y superfluid. Dirac and Weyl quasiparticles can be realized in the low-energy approximation near the two gapless nodes. Although the A-phase exists at a high pressure and high temperature in bulk, magnetic field and spatial confinement can be used to extend it to zero temperature at a low pressure. Searching for its chirality and time-reversal symmetry breaking will pave the way for further studies on its topological properties. Clues of the chirality have been found in a pioneering experiment studying electron bubbles in liquid ^{3}He.[33] A two-dimensional (2D) confinement can fix its orbital angular momentum normal to the substrate surface and manifest a one-dimensional edge current. An experimental search for such a chiral edge current has been proposed.[34]

There are some preliminary plans for superfluid ^{3}He research to be conducted using the ANDR at the SECUF. As mentioned previously, the Majorana state is predicted to naturally exist at the edge/surface of superfluid ^{3}He. The transport of Majorana along edges can carry heat, creating a temperature gradient. Owing to the spin–orbit interactions, the transport can be manipulated by a magnetic field. By using the experimental magnet of the ANDR at the SECUF, we expect to detect thermal transport and its variation under a magnetic field in order to find signatures of Majorana modes. The plan is still in a preliminary stage. Additional details will be confirmed during and after the construction of the ANDR.

3.2. FQHE

The Hall effect was discovered in 1879. It demonstrates that a voltage perpendicular to the current is established between two edges of a conductor when a magnetic field is present. The voltage is proportional to the field. Nearly a century later, in 1980, its quantized version was observed by von Klitzing *et al.* in a 2D electron gas (2DEG) system.[3] The perpendicular voltage, referred to as the Hall voltage, exhibits a stepwise increase with the magnetic field instead of a linear dependence. The corresponding Hall (transverse) resistance ρ_{xy} exhibits plateaus strictly at h/ne^2 for an integer n (see Fig. 13), which is described as the IQHE. When the applied magnetic field is sufficiently strong, electrons follow quantized circular orbitals with discrete energy levels $E_n = \hbar\omega_c(n+1/2)$. The energy levels are called Landau levels, and the energy gap $\hbar\omega_c$ is the cyclotron energy quantum. Landau levels remain discrete in the bulk but approach infinity near the edge. Correspondingly, the electron trajectories are complete circles in the bulk but incomplete at edges, giving rise to edge currents, as shown in Fig. 14. This can be explained by the fact that the Fermi level lies in the gap between two neighboring Landau levels in the bulk but cuts through the edge levels that bend upwards. The gap in which the Fermi level lies is determined by the filling factor. The number of the magnetic flux can be defined as $n_\Phi = B\cdot A/\Phi_0$, where B is the magnetic-field magnitude, A is the area of the 2DEG, and $\Phi_0 = hc/e$ is the flux quantum. The filling factor is given as the ratio of the electron number n_e to n_Φ : $\nu = n_e/n_\Phi = \rho\Phi_0/B$. Obviously, an increase in B reduces the filling factor.

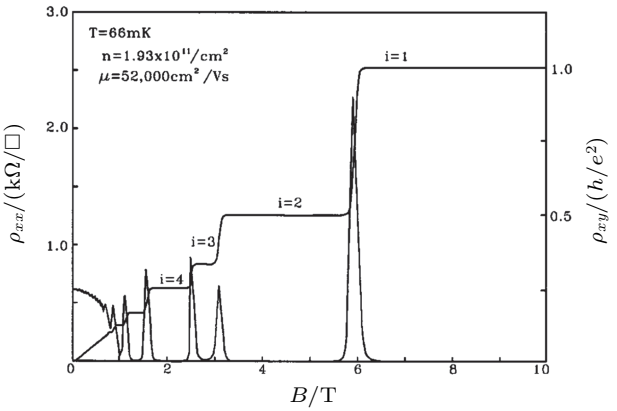


Fig. 13. Longitudinal and transverse resistances of the IQHE. (Regenerated from Ref. [61].)

The FQHE was discovered by Tsui, Stormer, and Gossard in 1982.[4] They observed that the Hall resistance is quantized at $h/\nu e^2$, where ν is a fractional number. The first observation was $\nu = 1/3$, and most of the states observed thus far have odd denominators, with a few exceptions. In contrast to the IQHE, where electrons are treated independently, electron–electron interactions are the main reason for the FQHE. A high mobility and low temperature are the key prerequisites for realizing the FQHE experimentally.

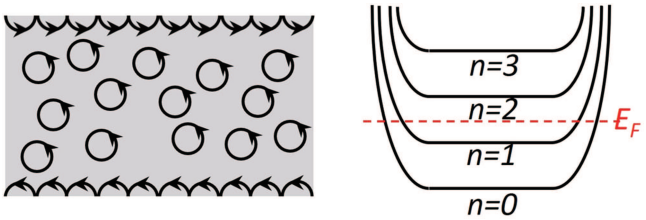


Fig. 14. (color online) (a) Discrete orbitals with an edge current. (b) Landau levels with distortion at the edges. When the Fermi level lies between two Landau levels, the bulk is insulating, but the edge is conducting.

Laughlin proposed a series of wave-functions that successfully describe states with $\nu = 1/k$ (k being odd integer).[35] Later, Jain proposed the composite-fermion approach and generalized the filling factor to a broader range.[36] A composite fermion consists of an electron attached to an

even number ($\alpha = 2p$) of flux quanta. The effective field felt by the composite fermions is $B^* = B - 2p\rho\Phi_0$, where ρ is the particle density. The effective filling factor for composite fermions is $\nu^* = \rho\Phi_0/|B^*| = 1/|\nu^{-1} - 2p|$, which gives $\nu = \nu^*/(2p\nu^* \pm 1)$, where $\pm$ indicates B^* being parallel/antiparallel to B. For an integer ν^*, these FQHE states can be viewed as the IQHE of composite fermions: the primary sequence of the FQHE. The FQHE of composite fermions, the secondary sequence, is also observed with ν^* as a fractional number. The hierarchical structure is shown in Fig. 15. In addition, flux quanta can be attached to holes, giving a series of filling factors $\nu = 1 - \nu^*/(2p\nu^* \pm 1)$. Together with the electron-flux composites, this covers most of the states for $\nu < 1$. The fractional filling can also occur at higher Landau levels, leading to $\nu = n + \tilde{\nu}$, where n is the number of fully filled Landau levels, and $\tilde{\nu} < 1$ is the effective filling factor on the partially filled level.

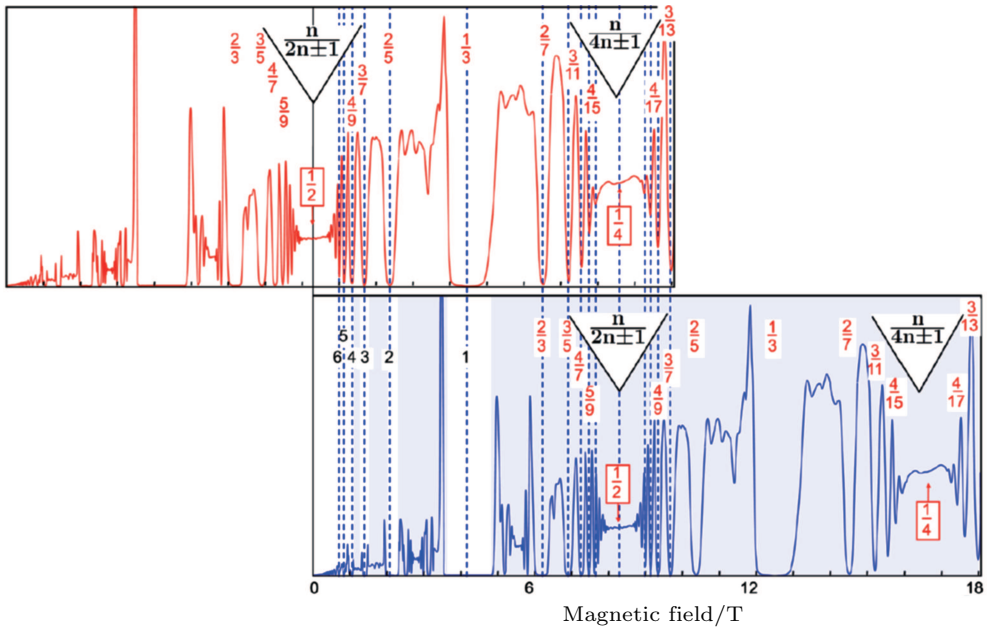


Fig. 15. (color online) Hierarchy of the FQHE. The structures of FQHE states near $\nu = 1/2$ and $1/4$ can match those near $\nu = 1$ and $1/2$, respectively, for the same set of data. (Regenerated from Ref. [62].)

The states in the aforementioned hierarchy all have odd denominators. However, ν with even denominators has also been observed. The most famous case is the $\nu = 5/2$ state,[37] where the lowest two Landau levels are occupied, and the third is half-filled. For the hierarchical filling factors, $\lim_{p\to 1, \nu^* \to +\infty}(\nu) = 1/2$. The half-filled state can be considered as a Fermi sea of composite fermions, which should not exhibit the FQHE.[38] Obviously, the FQHE at $\nu = 5/2$ is not simply a combination of two inert occupied and one half-filled Landau levels. One theory proposes that it is a "superconducting" state of composite fermions.[39] The formation of composite fermions overcomes the Coulomb repulsion and makes the interactions between composite fermions attractive, thus allowing pairing.[40] Several possible states have been proposed for $\nu = 5/2$. Moore and Read proposed a p-wave superconducting state of polarized composite fermions.[39,41] The Moore–Read state (also known as the Pfaffian state because of its mathematical description) follows non-Abelian statistics, potentially being useful for topological quantum computations. The anti-Pfaffian state, a particle–hole conjugate of the Pfaffian state, was proposed by Morf,[42] which also obeys non-Abelian statistics. A series of states obeying Abelian statistics have also been proposed, including one with d-wave pairing of composite fermions proposed by Haldane and Rezayi,[43] and the "331" state proposed by Halperin *et al.*[38,44] Wen proposed two possible states: the non-Abelian $U(1)\times SU_2(2)$ state[45,46] and the Abelian $K = 8$ state.[47]

The 5/2 state was first observed by Willett *et al.* in Hall measurements.[24] Subsequently, numerous experiments focused on its physical mechanism, owing to its exception to the hierarchical sequence and potential application in quantum computation. The effective fractional charge of $e/4$ has been observed in shot-noise measurements[48] and by coupling 2DEG with a single-electron transistor.[49] In addition, an interference experiment performed by Willett revealed Aharonov–Bohm oscillation with alternating periods of $e/2$ and $e/4$ [24] The alternation is considered as a demonstration of the non-Abelian property of the $e/4$ quasiparticles. Thus far, whether the $\nu = 5/2$ state is Abelian or non-Abelian remains an open question. Various experiments have been conducted to probe the statistics, but no concensus has been reached. Although all the proposed states have an effective fractional charge of $e/4$, the predicted quasiparticle interaction factor g differs in each model. The tunneling experiment is an

effective way to probe the interaction factor, and a previous investigation showed that the measured g favors the Abelian 331 state.[50] However, a recent experiment indicated that both the Abelian and non-Abelian states can be realized in the same device and switched by adjusting the confinement.[51] In addition to the magnetic field and temperature, the hydrostatic pressure affects the 5/2 state. It was observed that a quantum Hall nematic phase emerges at a certain applied pressure, causing the vanishing of the topological order and emergence of a broken symmetry.[52]

In addition to the 5/2 state, the 12/5 state was proposed to be non-Abelian by Read and Rezayi,[53,54] although it falls into the hierarchy in the form of $2+2/5$. They proposed "parafermion" states stemming from the $1/3$ Laughlin state and the $1/2$ Pfaffian state. The parafermion series features a filling factor of $\nu = \frac{k}{k+2}$. The filling factor $12/5$ can be viewed as $2+(1-3/5)$, meaning that it is the particle–hole conjugate state of $k=3$ with the lowest two Landau levels filled. Theories predicted that it hosts Fibonacci anyons, which permits universal topological quantum computations. The 12/5 state has been observed in a few experiments thus far.[55–57] However, its particle–hole conjugate, the 13/5 state, has not yet been observed.

The ultralow-temperature condition is essential for studies on the FQHE because the FQHE states should be isolated from the excited states by energy gaps larger than thermal energy $\Delta \gg k_B T$, but Δ is already small for some states. The Δ values of FQHE states near $\nu = 1/2$ and $\nu = 1/4$ exhibit a linear dependence[5] (see Fig. 16), which is consistent with the composite-fermion model: $\hbar\omega_c = \hbar eB^*/m^*$, where ω_c and m^* are the cyclotron frequency and the effective mass of the composite fermions, respectively; and B^* is the effective field that composite fermions feel. The linear dependencies shown in Fig. 16 have negative intercepts at $\nu = 1/2$ and $1/4$, owing to the broadening o the energy levels, which effectively reduces the energy gaps.

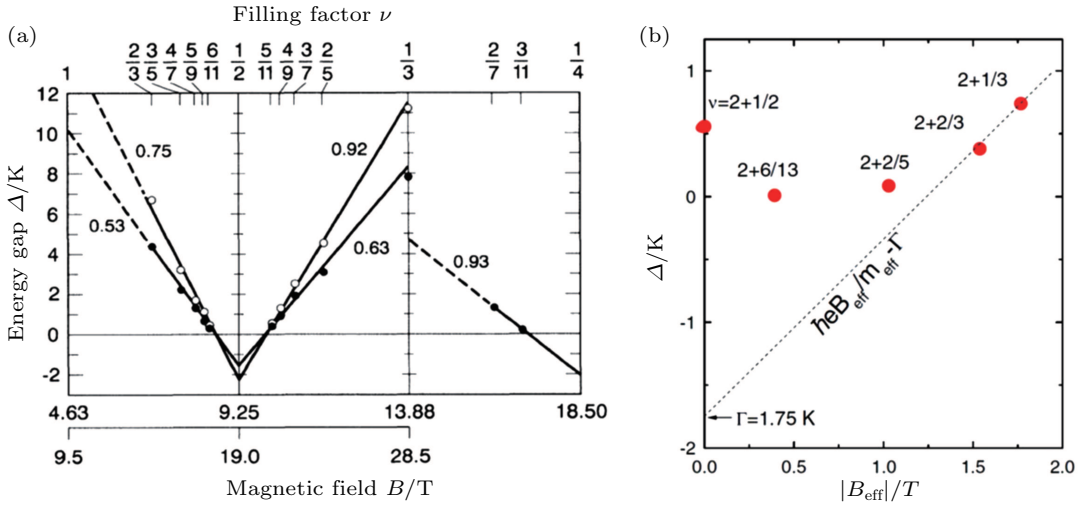


Fig. 16. (color online) (a) Gap energies with various filling factors for two samples, plotted with closed and open circles. The horizontal scale of the magnetic field has been shifted to match the filling factors between the two samples (regenerated from Ref. [5]). (b) Dependence of the energy gaps on the effective magnetic field $B_{\rm eff}$ for filling factors of $2+1/3 < \nu < 2+2/3$ (regenerated from Ref. [56]).

We are particularly interested in the two FQHE states that are the potential candidates for quantum computation: $\nu = 5/2$ and $12/5$. The $\nu = 5/2$ state is difficult to observe compared with other states such as $\nu = 1/3$. Its energy gap is strongly sample-dependent and sensitive to the electron density and mobility, as well as impurities. The energy gap can be as high as ~ 0.6 K for samples with high mobility but can also be undetectable for non-ideal samples at the other extreme. A usual requirement to observe such states is a mobility higher than 10^7 cm^2/V·s. This requires extremely strict or challenging methods and protocols for sample growth. Only a few labs worldwide can grow samples with such high quality. In addition to strict and challenging sample-preparation techniques, light-emitting diode illumination at low temperatures has been demonstrated as an effective way to increase the mobility. Compared with the 5/2 state, the 12/5 state is more elusive and fragile. Its energy gap is also dependent on the mobility and electron density, with the optimized value measured as approximately 80 mK.[56]

Because of the small energy gaps, experimental research on the FQHE, especially for the 5/2 and 12/5 states, requires ultralow-temperature conditions. Unfortunately, the coupling between electrons and lattices is weak at ultralow temperatures. For a dilution refrigerator without careful filtering, the electron temperature can be significantly higher than the base lattice temperature of ~ 10 mK. Various methods have been proposed and implemented to reduce the temperature limit, such as ^{3}He immersion and careful filtering along signal lines. Adiabatic nuclear demagnetization can cool the lattice to the sub-mK range. The low lattice temperature certainly helps in cooling electrons. However, careful signal filtering is necessary and of great importance. An electron temperature of

~ 4 mK was realized for a 2DEG sample in the 7/2 state (Δ was measured to be 22 mK) with the lattice at 0.5 mK using the ANDR at the Institute of Physics, Chinese Academy of Sciences. The filtering will be improved for the ANDR at the SECUF.

4. Conclusion and perspectives

With its proposed debut in 2023, the SECUF is designed as a large-scale comprehensive facility assembly for combining various extreme physical conditions. The ultralow temperature, as one of the most important extreme conditions for contemporary research in physical and chemical science, will serve as a hub to incorporate other extreme conditions, including an ultrahigh magnetic field, ultrahigh pressure, and ultrafast laser. In the previous section, we listed two topics that are typical candidates for sub-mK research. There are additional fields where the sub-mK condition is essential, including but not limited to quantum spin liquids, relaxation in glassy materials, and heavy fermions. We welcome all relevant research topics and scientists worldwide to utilize the sub-mK station at the SECUF.

References

[1] Kamerlingh Onnes H K 1911 *Comm. Phys. Lab. Univ. Leiden. Suppl.*
[2] Allen J F and Misner A D 1938 *Nature* **142** 643
[3] Klitzing K V, Dorda G and Pepper M 1980 *Phys. Rev. Lett.* **45** 494
[4] Tsui D C, Stormer H L and Gossard A C 1982 *Phys. Rev. Lett.* **48** 1559
[5] Du R R, Stormer H L, Tsui D C, Pfeiffer L N and West K W 1993 *Phys. Rev. Lett.* **70** 2944
[6] Lin X, Du R and Xie X 2014 *Natl. Sci. Rev.* **1** 564
[7] Das Sarma S, Gervais G and Zhou X 2010 *Phys. Rev. B* **82** 115330
[8] Dean C R, Piot B A, Hayden P, Das Sarma S, Gervais G, Pfeiffer L N and West K W 2008 *Phys. Rev. Lett.* **100** 146803
[9] Pobell F 2007 *Matter and Methods at Low Temperatures* (Springer Science & Business Media)
[10] Rusby R L, Durieux M, Reesink A L, Hudson R P, Schuster G, Kuhne M, Fogle W E, Soulen R J and Adams E D 2002 *J. Low Temp. Phys.* **126** 633
[11] Straty G C and Adams E D 1969 *Rev. Sci. Instrum.* **40** 1393
[12] Pobell F 1992 *J. Low Temp. Phys.* **87** 635
[13] Aalto M I, Berglund P M, Collan H K, Ehnholm G J, Gylling R G, Krusius M and Pickett G R 1972 *Cryogenics (Guildf)* **12** 184
[14] Eska G 1988 *J. Low Temp. Phys.* **73** 207
[15] Aalto M I, Collan H K, Gylling R G and Nores K O 1973 *Rev. Sci. Instrum.* **44** 1075
[16] Osheroff D D, Richardson R C and Lee D M 1972 *Phys. Rev. Lett.* **28** 885
[17] Osheroff D D, Gully W J, Richardson R C and Lee D M 1972 *Phys. Rev. Lett.* **29** 920
[18] Halperin W P, Archie C N, Rasmussen F B, Alvesalo T A and Richardson R C 1976 *Phys. Rev. B* **13** 2124
[19] Leggett A J 1975 *Rev. Mod. Phys.* **47** 331
[20] Volovik G E 2009 *The Universe in a Helium Droplet* (Oxford: Oxford University Press)
[21] Anderson P W 1960 *Physica* **26** S137
[22] Anderson P W and Morel P 1961 *Phys. Rev.* **123** 1911
[23] Balian R and Werthamer N R 1963 *Phys. Rev.* **131** 1553
[24] Willett R L, Pfeiffer L N and West K W 2009 *Proc. Natl. Acad. Sci. USA* **106** 8853
[25] Rice T M and Sigrist M 1995 *J. Phys.: Condens. Matter* **7** L643
[26] Ishida K, Mukuda H, Kitaoka Y, Asayama K, Mao Z Q, Mori Y and Maeno Y 1998 *Nature* **396** 658
[27] Mackenzie A P and Maeno Y 2003 *Rev. Mod. Phys.* **75** 657
[28] Qi X L, Hughes T L, Raghu S and Zhang S C 2009 *Phys. Rev. Lett.* **102** 187001
[29] Chung S B and Zhang S C 2009 *Phys. Rev. Lett.* **103** 235301
[30] Aoki Y, Wada Y, Saitoh M, Nomura R, Okuda Y, Nagato Y, Yamamoto M, Higashitani S and Nagai K 2005 *Phys. Rev. Lett.* **95** 075301
[31] Davis J P, Pollanen J, Choi H, Sauls J A, Halperin W P and Vorontsov A B 2008 *Phys. Rev. Lett.* **101** 085301
[32] Choi H, Davis J P, Pollanen J and Halperin W P 2006 *Phys. Rev. Lett.* **96** 125301
[33] Ikegami H, Tsutsumi Y and Kono K 2013 *Science* **341** 59
[34] Byun H, Jeong J, Kim K, Kim S G, Shim S B, Suh J and Choi H 2016 arXiv:160907641
[35] Laughlin R B 1983 *Phys. Rev. Lett.* **50** 1395
[36] Jain J K 1989 *Phys. Rev. Lett.* **63** 199
[37] Willett R, Eisenstein J P, Störmer H L, Tsui D C, Gossard A C and English J H 1987 *Phys. Rev. Lett.* **59** 1776
[38] Halperin B I, Lee P A and Read N 1993 *Phys. Rev. B* **47** 7312
[39] Read N and Green D 2000 *Phys. Rev. B* **61** 10267
[40] Scarola V W, Park K and Jain J K 2000 *Nature* **406** 863
[41] Moore G and Read N 1991 *Nucl. Phys. B* **360** 362
[42] Morf R H 1998 *Phys. Rev. Lett.* **80** 1505
[43] Haldane F D M and Rezayi E H 1988 *Phys. Rev. Lett.* **60** 956
[44] Halperin B I 1973 *Helv. Phys. Acta* **56** 75
[45] Wen X G and Niu Q 1990 *Phys. Rev. B* **41** 9377
[46] Wen X G 1991 *Phys. Rev. Lett.* **66** 802
[47] Wen X G and Zee A 1992 *Phys. Rev. B* **46** 2290
[48] Dolev M, Heiblum M, Umansky V, Stern A and Mahalu D 2008 *Nature* **452** 829
[49] Venkatachalam V, Yacoby A, Pfeiffer L and West K 2011 *Nature* **469** 185
[50] Lin X, Dillard C, Kastner M A, Pfeiffer L N and West K W 2012 *Phys. Rev. B* **85** 165321
[51] Fu H, Wang P, Shan P, Xiong L, Pfeiffer L N, West K, Kastner M A and Lin X 2016 *Proc. Natl. Acad. Sci. USA* **113** 12386
[52] Samkharadze N, Schreiber K A, Gardner G C, Manfra M J, Fradkin E and Csáthy G A 2016 *Nat. Phys.* **12** 191
[53] Read N and Rezayi E 1999 *Phys. Rev. B* **59** 8084
[54] Rezayi E H and Read N 2009 *Phys. Rev. B* **79** 075306
[55] Xia J S, Pan W, Vicente C L, Adams E D, Sullivan N S, Stormer H L, Tsui D C, Pfeiffer L N, Baldwin K W and West K W 2004 *Phys. Rev. Lett.* **93** 176809
[56] Kumar A, Csathy G A, Manfra M J, Pfeiffer L N and West K W 2010 *Phys. Rev. Lett.* **105** 246808
[57] Zhang C, Huan C, Xia J S, Sullivan N S, Pan W, Baldwin K W, West K W, Pfeiffer L N and Tsui D C 2012 *Phys. Rev. B* **85** 241302
[58] Betts D S 1989 *An Introduction to Millikelvin Technology* (Cambridge: Cambridge University Press)
[59] Seribner R A, Panezyk M F and Adams E D 1969 *J. Low Temp. Phys.* **1** 313
[60] Grilly E 1971 *J. Low Temp. Phys.* **4** 615
[61] Tsui D C 1999 *Rev. Mod. Phys.* **71** 891
[62] Jain J K 2014 *Indian J. Phys.* **88** 915